Dynamics of Seeded Aβ_{40}-Fibril Growth from Atomistic MD Simulations: Kinetic Trapping and Reduced Water Mobility in the Locking Step

Nadine Schwierz[a,*], Christina V. Frost[b], Phillip L. Geissler[a] and Martin Zacharias[b]

[a]*Chemistry Department, University of California, Berkeley, California 94720, United States;* [b]*Physik Department, Technische Universität München, 85748 Garching, Germany;* [*]*nschwierz@berkeley.edu*

(Dated: December 22, 2015)

Abstract

Filamentous β-amyloid aggregates are crucial for the pathology of Alzheimer's disease. Despite the tremendous biomedical importance, the molecular pathway of growth propagation is not completely understood and remains challenging to investigate by simulations due to the long time scales involved. Here, we apply extensive all-atom molecular dynamics simulations in explicit water to obtain free energy profiles and kinetic information from position-dependent diffusion profiles for three different Aβ_{9-40}-growth processes: Fibril elongation by single monomers at the structurally unequal filament tips and association of larger filament fragments. Our approach provides insight into the molecular steps of the kinetic pathway and allows close agreement with experimental binding free energies and macroscopic growth rates. Water plays a decisive role and solvent entropy is identified as the main driving force for assembly. Fibril growth is disfavored energetically due to cancellation of direct peptide-peptide interactions and solvation effects. The kinetics of growth is consistent with the characteristic dock/lock mechanism and docking is at least two orders of magnitude faster. During initial docking, interactions are mediated by transient non-native hydrogen bonds which efficiently catch the incoming monomer or fragment already at separations of about 3 nm. In subsequent locking, the dynamics is much slower due to formation of kinetically trapped conformations caused by long-lived non-native hydrogen bonds. Fibril growth additionally requires collective motion of water molecules to create a dry binding interface. Fibril growth is further retarded due to reduced mobility of the involved hydration water, evident from a two-fold reduction of the diffusion coefficient.

1

INTRODUCTION

Self-assembly of peptides into ordered amyloid fibrils is associated with several neurode-generative diseases including Parkinson's, Huntington's and Alzheimer's disease [1–3]. In Alzheimer's disease, the key component of the pathological aggregates is the so called $A\beta$ peptide resulting from the cleavage of the amyloid precursor protein, with $A\beta_{1-40}$ being the most abundant isoform. Despite the tremendous biomedical importance of amyloid fibrils, the molecular mechanism and the dynamic pathway involved in their formation has remained elusive and challenging to investigate in experiments and simulations. At the same time, the quantitative understanding of the mechanism driving the transition from monomer to fibril is essential for an efficient design of tailored drugs.

The characteristic cross-β structure of $A\beta_{1-40}$ fibrils has been resolved by NMR exper-iments [4, 5] and the structural stability of the fibrils has been characterized [6, 7]. For several subfragments of the $A\beta_{1-40}$ peptide, the formation of stable amyloid fibrils has been observed, including $A\beta_{9-40}$ which lacks the first 8 N-terminal residues [7]. The formation of $A\beta$ fibrils involves a nucleation step and a subsequent elongation process in which $A\beta$ monomers are added to the fibril tips. The elongation process has been studied intensively in kinetic experiments [8–16]. Based on these experimental results, a two-step elongation process has been suggested [8, 10, 17]. It involves rapid association of the unstructured monomer to the fibril (docking), followed by significantly slower conformational rearrange-ments to precisely accommodate the monomer into the underlying ordered fibril structure (locking). The second distinct mechanism that is essential for controlling the kinetics of growth is fibril breakage, which increases the number of ends acting as new elongation sites [18, 19]. The design of inhibitors of fibril formation, as well as the design of fibril based ma-terials, requires a detailed understanding of the mechanism of fibril propagation at atomic detail.

To complement kinetic experiments, molecular simulations are well suited to provide insight into the role of sequence, water and specific interactions underlying the elementary kinetic steps in the aggregation pathway. However, due to the slow time scales involved in fibril association and especially in dissociation in combination with large system sizes, simulations of the full kinetic pathway in all-atom resolution and with explicit water are tremendously challenging. For example, experiments indicate that the timescale for $A\beta$

monomer dissociation from fibrils occurs on the order of seconds to several minutes [8, 10, 11]. Still, significant insight into the mechanism of fibril formation can be gained from coarse-grained [20–22] and implicit water simulations [23, 24] as well as from atomistic simulations of short fragments of the Aβ peptide and other proteins [17, 25, 26]. In order to overcome the computational time scale limit, hybrid-approaches with a united atom representation of the peptides and a coarse-grained model of the solvent have been employed [27]. Implicit solvent simulations [24] and hybrid-approaches [27] allow extensive sampling, however, the role of solvent molecules for the association approach and the balance between (solvent) entropic and energetic contributions to amyloid formation may not be accurately represented. Alternatively, it is also possible to employ advanced sampling techniques like transition path sampling [28], or combine simulations with experimental data obtained from two-dimensional spectroscopy [29].

In the present study, we use extensive atomistic simulations in explicit solvent and a two-step approach to resolve both thermodynamic and kinetic aspects of fibril growth. This allows us to investigate the elementary steps of different fibril growth processes with atomistic resolution and to gain insight into the dynamic pathway, using the Aβ_{9-40} peptide as a model system. In the first step of our approach, we calculate the free energy profile for fibril elongation by a single monomer at the two asymmetric filament tips and for the association of two larger fibril fragments. We further characterize the molecular steps underlying the free energy profiles by elucidating associated conformational changes, formation and breakage of native and non-native hydrogen bonds and analyzing the role of water molecules involved in the assembly process. During the initial docking phase, the approaching monomer or fragment starts to interact with the filament already at a peptide-tip distance > 2.5 nm. These initial interactions are mediated by transient, mostly non-native hydrogen bonds and other non-native contacts. Formation of such contacts is possible due to the large conformational flexibility of the peptides.

The forces driving filament formation are investigated in a detailed enthalpy/entropy decomposition. Surprisingly, the calculations indicate that filament elongation is overall energetically disfavored but favored entropically, despite the large reduction of possible peptide conformational freedom upon association. However, monomer binding to the filament tip has also a substantial influence on the aqueous solvent structure, resulting in a dominant role of solvent entropy as the main driving force for assembly.

In the second step of our approach, we extract kinetic information from our simulations by determining the position-dependent diffusion profile of the approaching monomer or fibril fragment. Starting in the initial docking phase, the diffusivity rapidly decreases upon further approach to the bound state, thus limiting the speed of the growth process. In our theoretical framework, a combination of diffusion and free energy profile uniquely determines the dynamics of fibril growth and allow us to estimate kinetic rates. The dissociation rates calculated from our approach agree well with experimental results and the predicted kinetic pathway is consistent with the dock/lock mechanism suggested from kinetic experiments. A detailed analysis of the motion of water molecules close to the binding site reveals a 2-fold reduction of water mobility indicating a substantial contribution of water-mediated interactions to the association process. Finally, we elucidate the molecular mechanism underlying the slow dynamics in the limiting locking step.

METHODS

Atomistic model and simulation setup: In this work, we study atomistic-level models of molecular filaments composed of wild type $A\beta_{9-40}$ peptides. The N-terminal residues 1-8 are neglected since they are structurally disordered and not necessary for growth [7]. The filament structure employed is the one determined by Petkova et al. [4, 5] (PDB code 2LMN with a +2 staggering). In order to investigate the stability of the model systems, we perform 100 ns NPT simulations at 5 different temperatures for filaments consisting of a varying number of peptides (for details see Supporting Information). The stability analysis indicates that filaments with more than 4 peptides form a stable cross-β structure and a constant gain in free energy is expected for further addition of new monomers to the filament [22]. Our initial filament model consists of 12 monomers and is built by selecting one β-hairpin peptide from the experimental NMR-structure [4, 5] and stringing additional peptide copies repeatedly along the filament axis, with an inter-peptide separation of 0.48 nm. The amino acid termini are capped using an uncharged amino group at the N-terminus and an uncharged carboxyl group at the C-terminus. In our model, residues K16 and K28 are positively charged and residues E11, E22 and D23 are negatively charged based on neutral pH, physiological salt concentration and the pK values of the amino acids. This results in one excess negative charge for each peptide. The force field parameters for the peptides are

4

taken from CHARMM version C27 [30]. Initially, the filament is placed in the simulation box before filling in TIP3P water molecules [31]. In order to neutralize the system, 0.15 M NaCl is added to the water phase, leading to a system size of about 60,000 atoms. The simulation box has the size $L_x = 8$ nm, $L_y = 5$ nm and $L_z = 14.5$ nm. We investigate the elongation/dissociation of a filament by one peptide at the even tip (N-terminal solvent exposed), at the odd tip (C-terminal exposed) and the association/fragmentation of two hexamers (see Figure 1A). All systems contain 12 Aβ_{9-40}-peptides in total.

To monitor the progress in binding, we use the separation coordinate ζ, defined by the center of mass distance along the filament axis between the monomer (hexamer) and the first peptide at the respective filament tip. The motion of the monomer and hexamer perpendicular to ζ remains unrestrained. Positional restraints are applied to the last peptide at the filament tip where the elongation process takes place. These restraints prevent twisting motions, thereby mimicking larger filaments with a structurally stable binding site.

In order to generate starting conformations for the umbrella sampling simulations, an additional idealized U-shaped monomer or hexamer is placed into the simulation box and aligned along the filament axis using an initial separation of $n \times d_n + d_0$, where n is the window number, d_n the window spacing and $d_0 = 0.48$ nm the initial peptide separation in the NMR structure. We choose this lateral displacement method to generate the umbrella starting conformations since the commonly used pulling algorithm requires breaking of hydrogen-bonds in adjacent $\beta-$sheets. In order to generate useful starting conformations, very small pulling velocities ($v \ll 0.1$ m/s) and long subsequent equilibration would be necessary [32]. On the other hand, the β-hairpin conformation of the monomer used here provides a useful starting conformation since it is suggested to be an on-pathway intermediate structure [27].

The molecular dynamics simulations at fixed particle number N, pressure P and temperature T are performed using the Gromacs simulation package, version 4.6.1 [33]. Periodic boundary conditions are applied and the particle-mesh Ewald method is used for the periodic treatment of Coulomb interactions. The bonds to hydrogen atoms are constrained by the LINCS algorithm [34] and a 2 fs time step is used. To equilibrate the system, we first perform an energy minimization with the steepest descent algorithm. We employ a 200 ps NVT and NPT simulation as pre-equilibration using the Berendsen scheme. In the production run, we perform umbrella sampling simulations with 33 windows along the filament axis, employing Nosé-Hoover temperature coupling with a time constant of $\tau_T = 0.5s^{-1}$

and isotropic Parrinello-Rahman pressure coupling with a time constant of $\tau_p = 5s^{-1}$. We use a window width of 0.1 nm for the separation range $\zeta < 2$ nm, and 0.2 nm for larger distances. For all windows, an umbrella force constant of $k_\zeta = 1000$ kJ/(mol nm^2) is used. For elongation at the odd tip and fragmentation, umbrella simulations are performed for 100 ns per window.

In order to test the convergence of the potentials of mean force (PMF), the elongation simulations at the even filament tip have an extended duration of 150 ns in each window. The simulation data are divided into two blocks and the PMFs are calculated separately from each block. The resulting PMFs are in good agreement and the errors amount to ± 2.2 $k_\mathrm{B}T$ for elongation at the even tip, ± 3 $k_\mathrm{B}T$ for elongation at the odd tip and ± 2.9 $k_\mathrm{B}T$ for fragmentation. The convergence of the umbrella simulations is discussed in greater detail in the Supporting Information. The PMFs are calculated using the weighted histogram analysis method [35], discarding the first 10 ns for equilibration.

Thermodynamic analysis: Conformational transitions are quantified using different order parameters: The distance root mean square deviation (dRMSD) is calculated for all C$_\alpha$ atoms with respect to the idealized β-hairpin conformation of bound monomers. To measure the compactness of the monomer, the radius of gyration R$_G$ is calculated with respect to the center of mass of the molecule. Both order parameters are calculated as average over the last 50 ns in each umbrella window, and error bars correspond to standard deviations. Changes in secondary structure including the content of β-sheet and coil structure are calculated using the DSSP algorithm [36].

The stability of the cross-β structure upon fragmentation is quantified using the nematic order parameter $\overline{P}_2$ [37]. $\overline{P}_2$ is calculated using the Wordom analysis package [38]. For the N-terminal (NT), the atom vector corresponds to the C_α atom vector between residues 17 and 21. For the C-terminal (CT), it corresponds to the vector between residues 32 and 36, similar to a work of Buchete and coworkers [6]. The two peripheral monomers are omitted from analysis due to considerable conformational fluctuations.

The structures resulting from the umbrella simulations are clustered using the average-linkage algorithm and the dRMSD of all C$_\alpha$ atoms after removing rotation and translation with respect to the heavy atoms as the distance for the analysis. The average-linkage algorithm is used for clustering, as it was shown to be one of the most useful algorithms for analyzing molecular dynamics trajectories [39]. The simulation snapshots depict the

conformation that corresponds to the representative of the largest cluster. For the analysis of hydrogen bonds, the standard hydrogen bond definition of Gromacs is used. It corresponds to a donor-acceptor distance < 0.35 nm and donor-hydrogen-acceptor angle $< 30°$ [33].

The azimuthal reorientation correlation of the peptide during the umbrella sampling simulations is investigated using the Gromacs gprincipal tool. In each frame, the principle components of the monomer's moment of inertia tensor are calculated and the orientation of the major axis with respect to a fibril associated axis is used for calculating time fluctuations and autocorrelation functions.

The total enthalpy and its individual contributions due to peptide-peptide, peptide-solvent and solvent-solvent interactions are extracted as time averages for each umbrella window, discarding the first 50 ns for equilibration. In order to obtain the enthalpy difference between the bound and the unbound state, the windows are split accordingly, neglecting the intermediate region. Hereby, we define the bound region for peptide-fibril separations < 0.65 nm and the unbound region for separations > 3.2 nm. The average energy of each state is then calculated as a weighted average over all bound and unbound conformations. Statistical uncertainties are determined using the error estimate method [40]. Insight into the various energetic contributions stemming from interactions of peptide (P) and solvent (S) can be gained from the simulations. In a simulation rerun, the system is divided into the individual components and the energies of the individual groups are calculated. The individual contributions sum up to the total enthalpy according to $H \approx U_{\mathrm{PP}} + U_{\mathrm{SS}} + U_{\mathrm{PS}} + pV$. The small group of ions is omitted from analysis. Note that a further decomposition of the pV contribution is not feasible. However, it makes up only an negligibly small contribution of about 0.1 $k_{\mathrm{B}}T$ to the total enthalpy difference. Further information on the energy decomposition is provided in the Supporting Information.

Additional unbiased 300 ns simulations are performed to analyze the motion of the water molecules in the cavity of the filament. The lateral diffusion coefficient is calculated from the mean square displacement of the x- and y-coordinates of the water oxygens (see Supporting Information for details).

Position-dependent diffusion profile: In the following, we model the dynamics of fibril growth as diffusion in a one-dimensional free energy profile. We assume that the stochastic time evolution of the peptide-filament separation coordinate ζ is given by the one dimensional

Fokker-Planck (FP) equation [41]

$$\frac{\partial}{\partial t}\Psi(\zeta,t) = \frac{\partial}{\partial \zeta}D(\zeta)e^{-\beta G(\zeta)}\frac{\partial}{\partial \zeta}\Psi(\zeta,t)e^{\beta G(\zeta)} \tag{1}$$

where $\Psi(\zeta,t)$ is the probability distribution of the separation ζ between peptide and fibril at time t, $D(\zeta)$ is the position-dependent diffusion profile, $G(\zeta)$ is the free energy profile along ζ calculated from umbrella sampling simulations and $\beta = 1/k_{\mathrm{B}}T$. Note that as a consequence of the projection of the high dimensional dynamics onto our one-dimensional separation coordinate, the diffusion coefficient $D(\zeta)$ depends on the value of ζ. Changes in the diffusion coefficient are therefore a signature of the degrees of freedom perpendicular to ζ that influence the kinetics.

For a sufficiently narrow harmonic umbrella potential, the position-dependent diffusion profile can be calculated directly from the simulation data in each umbrella window [42, 43]

$$D(\zeta) = \frac{\sigma^2(\zeta)}{\tau} \tag{2}$$

where $\sigma^2(\zeta) = \langle\zeta^2\rangle - \langle\zeta\rangle^2$ is the variance and τ is the integrated normalized autocorrelation function $\tilde{C}(t) = \langle\zeta(t)\zeta(0)\rangle - \langle\zeta(t)\rangle\langle\zeta(0)\rangle/\sigma^2(\zeta)$. From a simulation trajectory with n data points ζ_i, the average separation $\overline{\zeta} = \sum\zeta_i/n$ is used to replace $\langle\zeta\rangle$. Note that the estimation of $\langle\zeta\rangle$, $C(t)$ and τ is only reliable if $C(t)$ vanishes on timescales shorter than the simulation time. Under this assumption τ can be calculated from [44]

$$\tau \approx \left[\frac{n\sigma^2(\overline{\zeta})}{\sigma^2(\zeta)} - 1\right]\Delta t/2 \tag{3}$$

where Δt is the time interval between the data points. A reliable method to calculate the variance of the average separation $\sigma^2(\overline{\zeta})$ is block averaging developed by Petersen and coworkers [44]. Alternatively, $\sigma^2(\overline{\zeta})$ can be calculated from the error estimate method assuming a double exponential decay of the correlation function [40]. The difference between the error estimate method and the result from block averaging using 4 data blocks is used to determine the error of $D(\zeta)$. Further details on the calculation of $\sigma^2(\overline{\zeta})$ and the correlation function are given in the Supporting Information.

In general, our two-step approach allows us to separate effects arising from the curvature in the free energy profile and the local diffusion coefficient. Note also that the diffusion coefficient could in principle be calculated from the variance $\sigma^2(\Delta t) \approx 2D(\zeta)\Delta t$ after a short time Δt. However, for the one-dimensional Fokker-Planck equation to be valid, the projected dynamics has to be Markovian, i.e. without memory. In order to minimize possible

errors due to memory effects, we use the full dataset of trajectories (100 ns per window) for calculating $D(\zeta)$.

Rescaling of the free energy profile: Using a combination of free energy and diffusion profiles results in a kinetic quasi-universality. Specifically, the Fokker-Planck equation (Eq. 1) is invariant under rescaling of the coordinate $q = q(\zeta)$, provided that the functions Ψ, G and D are rescaled simultaneously [45–47]. Conversely, a constant diffusion profile $\tilde{D}(\zeta) = D_0$ can be obtained by choosing

$$q(\zeta) = \int_{\zeta_0}^{\zeta} \mathrm{d}\zeta' \sqrt{D_0/D(\zeta')} \tag{4}$$

and rescaling the free energy profile $\tilde{G}(q) = G(\zeta) - \ln(D(\zeta)/D_0)/2\beta$. With this rescaling, regions in which the kinetics along the original separation coordinate ζ are slow become stretched in the rescaled coordinate $q(\zeta)$. More importantly, the rescaled free energy profile now contains the full information on the kinetics and may show intermediate states that remained hidden in the original coordinate ζ.

Binding free energy, mean first passage time and rate constants: We consider the binding process $F + P \leftrightarrow FP$ of a filament (F) and peptide (P) in dilute solution. Its equilibrium state obeys a law of mass action

$$k_{\mathrm{EQ}} = \frac{[FP]}{[F][P]} \tag{5}$$

where $[i]$ denotes the concentration of species i. The equilibrium constant k_{EQ} for peptide binding can be computed from simulations through the reversible work function $w(x, y, \zeta)$ for the vector separation between filament and peptide (with Cartesian components ζ, x, and y) [48]:

$$k_{\mathrm{EQ}} = \int \mathrm{d}x \int \mathrm{d}y \int \mathrm{d}\zeta \ e^{-\beta w(x,y,\zeta)} \theta_{\mathrm{b}}(x, y, \zeta), \tag{6}$$

where we have set $w = 0$ at infinite separation. The characteristic function $\theta_{\mathrm{b}}(x, y, \zeta)$ is unity for values of x, y, and ζ corresponding to the bound state, and vanishes otherwise. Provided that $w(x, y, \zeta)$ possesses a deep minimum at contact and decays over microscopic length scales (as confirmed by simulation results described later), the detailed choice of $\theta_{\mathrm{b}}(x, y, \zeta)$ is unimportant. We require only that the volume in which $\theta_{\mathrm{b}} = 1$ encompasses typical fluctuations of the bound state, and that it be microscopic in scale. With this freedom, we make the convenient choice that $\theta_{\mathrm{b}} = 1$ only when $-L_x/2 < x < L_x/2$, $-L_y/2 < y < L_y/2$, and $\zeta_B < \zeta < \zeta_S$, where ζ_B is the separation at minimum $G(\zeta)$ and ζ_S is the smallest

separation for which $G(\zeta) \approx 0$. This volume spans the lateral dimensions of our simulation cell and includes all points at which $w(x, y, \zeta)$ is appreciably nonzero. The calculation of k_{EQ} then reduces to a simple integral,

$$k_{\text{EQ}} = L_x L_y \int_{\zeta_B}^{\zeta_S} \mathrm{d}\zeta \, \frac{P_{\text{sim}}(\zeta)}{P_{\text{sim}}(\zeta_S)}, \tag{7}$$

of the separation probability distribution $P_{\text{sim}}(\zeta)$ obtained from simulations within our microscopic cell. We discuss this distribution in terms of the corresponding free energy profile $G(\zeta) = k_{\text{B}} T \ln[P_{\text{sim}}(\zeta)/P_{\text{sim}}(\zeta_S)]$ for reversible changes in peptide-filament separation. To facilitate comparison with experiments, we compute as well a free energy of binding,

$$\Delta G_{\text{Bind}} = k_{\text{B}} T \ln \left[c^0 k_{\text{EQ}} \right] \tag{8}$$

whose value depends on the arbitrary choice of standard state concentration c^0. Consistent with experimental reports, we choose $c^0 = 1 \, \text{mol/L} = (1.661 \, \text{nm}^3)^{-1}$. The binding and unbinding rate constants for a monomer or hexamer at the filament tip can be related to the dynamics of ζ at microscopically small separation. Specifically, these kinetic parameters are determined by waiting times for binding and escape when ζ is confined to the interval $\zeta_B < \zeta < \zeta_S$. For the diffusive dynamics of Eq. 1 subject to these boundary conditions, the mean first passage time τ_{ub} for unbinding (i.e., the average time required for trajectories initiated at $\zeta = \zeta_B$ to first reach ζ_S) is given by[49]

$$\tau_{\text{ub}} = \int_{\zeta_B}^{\zeta_S} \mathrm{d}\zeta' \frac{e^{\beta G(\zeta')}}{D(\zeta')} \int_{\zeta_B}^{\zeta'} \mathrm{d}\zeta'' e^{-\beta G(\zeta'')}. \tag{9}$$

The mean first passage time τ_{b} for binding can similarly be determined as

$$\tau_{\text{b}} = \int_{\zeta_B}^{\zeta_S} \mathrm{d}\zeta' \frac{e^{\beta G(\zeta')}}{D(\zeta')} \int_{\zeta'}^{\zeta_S} \mathrm{d}\zeta'' e^{-\beta G(\zeta'')}. \tag{10}$$

From these microscopic mean first passage times and the equilibrium constant (Eq. 7), we can identify microscopic rate constants for binding and unbinding valid for reaction within a small cage of radius ζ_S around the filament

$$k_{\text{off}}^{\text{micro}} = \frac{1}{\tau_{\text{ub}}}; \quad k_+^{\text{micro}} = k_{\text{EQ}} k_{\text{off}}^{\text{micro}}. \tag{11}$$

The concentration $[F_j]$ of fibrils of length j is expected to follow a phenomenological rate equation

$$\frac{\mathrm{d}[F_j]}{\mathrm{d}t} = -k_+[M][F_j] + k_{\text{off}}[F_{j+1}] + k_+[M][F_{j-1}] - k_{\text{off}}[F_j] \tag{12}$$

10

In order to establish a connection between the experimentally accessible macroscopic rates k_+ and k_{off} and the microscopic rates based on first passage times, we must account for the time-dependent spatial distribution of the peptides. By balancing the flux of peptides at steady state, we can derive expressions for the overall rate constants k_+ and k_{off} [50]

$$k_+ = \frac{k_+^{\text{micro}}}{1 + \frac{k_+^{\text{micro}}}{4\pi D \zeta_S}}; \quad k_{\text{off}} = \frac{k_{\text{off}}^{\text{micro}}}{1 + \frac{k_+^{\text{micro}}}{4\pi D \zeta_S}}. \tag{13}$$

In the limit $k_+^{\text{micro}} \ll 4\pi D \zeta_S$, i.e. if the binding of the peptide is much slower than the rate of filament-peptide encounters, the overall rate is given by $k = k^{\text{micro}}$. In the limit $k_+^{\text{micro}} \gg 4\pi D \zeta_S$, i.e if the binding is fast compared to the encounter rate by diffusion, the rate is diffusion controlled. The overall rate is then given by $k = 4\pi D \zeta_S$. Table I lists all computed rates including the diffusion limit for $A\beta_{9-40}$ filament growth by addition of a single monomer or by the association of two hexamer fragments. Note that we neglect the diffusion of the fibril for monomer binding (D corresponds to the calculated diffusion coefficient for a single monomer in bulk). For fragmentation D is the sum of diffusion coefficients of the two hexamer fragments in bulk.

In general, the kinetics of fibril growth can be modeled using a master equation description, in which the fibers can undergo end-to-end association, elongation, fragmentation, and primary nucleation. To ensure that the entropy production rate is finite, any consistent model for growth must consider all possible reaction pathways that lead to the formation of fibrils of a certain length together with their reverse processes to obey detailed balance. [19]. The requirement to satisfy detailed balance allows us to determine the rate of primary nucleation to be $k_n[M]^{n_c}$ based on the rates of elongation and fragmentation obtained from our simulations according to [19]

$$k_n = \frac{2k_{\text{off}}}{\hat{k}_{\text{EQ}}} (k_{\text{EQ}})^{n_c}. \tag{14}$$

From experimental data, the reaction order for nucleation has been estimated as $n_c = 2$ [14], a value we adopt as well for the purpose of comparison. Here, $\hat{k}_{\text{EQ}}$ is the equilibrium constant for association/fragmentation of large filament fragments.

11

RESULTS AND DISCUSSION

The present study focuses on the three different growth processes that are relevant for the kinetics of $A\beta_{9-40}$ filaments growth propagation: the elongation by a single monomer at the two structurally different filament tips and the association of two hexamers (see illustration in Figure 1A). The filament structure exhibits a U-shaped, strand-loop-strand (β-hairpin) conformation characteristic for $A\beta$ fibrils [4, 5] and is illustrated in Figure 1B. According to its secondary structure, each peptide is divided into three regions: The N-terminal (NT) β-strand including the central hydrophobic region L17-A21, the loop region including the D23-K28 salt-bridge, and the C-terminal (CT) β-strand. Due to the internal +2 staggering of the β-sheet, the two filament ends are not identical: On one tip, the NT region is left unpaired and solvent exposed (even tip); at the other tip, the CT region is left unpaired (odd tip). In the following, "filament" refers to structures with peptides arranged in one molecular layer along the filament axis (see Figure 1). "Fibril" refers to structures consisting of two or more filaments arranged in several layers.

In the following sections, we first present the free energy profiles for filament growth by monomer addition at both filament ends and by association of larger fragments. The underlying structural transitions are then characterized by analyzing the conformational changes, the formation and breakage of native and non-native hydrogen bonds as well as the collective motion of water molecules to create a dry binding interface upon assembly. The forces driving filament formation are subsequently analyzed in an energy/entropy decomposition. Finally, we present the calculated diffusion profiles and rescaled free energy profiles, which contain the full kinetic information and reveal characteristics of the dock/lock mechanism.

Free energy profile for filament growth: Figure 2 shows the free energy profile $G(\zeta)$ for the three different growth processes along the peptide-filament separation ζ: For filament elongation by a $A\beta$ monomers at the even and odd fibril tip (Figure 2A, B) and for association of two hexamers (Figure 2C). The binding affinities are calculated from the equilibrium constants (Eq. 7, 8), adopting the standard state convention $c^0 = 1$ mol/L. The calculated binding affinities amount to 22.8 ± 2.2 $k_{\mathrm{B}}T$ and 24.9± 3 $k_{\mathrm{B}}T$ for filament elongation at the even and odd tip, respectively. Within the estimated error, the results agree with the expectation that both free energy changes should be identical since initial and final states of the association process at either tip are identical. The calculated affinities are more favorable,

12

but still comparable to the experimental value of 15.2 k_BT [11] and match the experimental value much more closely than previous all-atom simulations (85.2 k_BT)[51]. An analysis of the orientational and rotational correlation of the monomer relative to the fibril tip reveals sampling of a large variety of relative geometries and rapid rotation of the monomer compared to the time scale of the umbrella sampling simulations (Supporting Information, Figure S6).

For association of two hexamers, the calculated binding affinity for this process is significantly larger (47.3 ± 2.9 k_BT) compared to monomer association at the filament tips.

For all three association processes, the free energy profiles can be divided into three regions: The locked region in which predominantly native hydrogen bonds are formed, an intermediate region in which docking occurs by the formation of non-native hydrogen bonds, and the unbound region. The latter corresponds to the absence of interactions between the monomer/hexamer and filament at large distances, resulting in a constant profile within statistical noise ($\zeta > \zeta_S$). In the docking region, the profiles decrease continuously as the monomer/hexamer approaches the filament ($\zeta_S > \zeta > \zeta_C$). ζ_C indicates the crossover from the fast docking to the much slower locking and will be discussed in detail further below. Finally, at small separations, all free energy profiles show a pronounced minimum at the peptide-peptide (or hexamer-hexamer) separation found in the NMR structure [4, 5] ($\zeta_B = 0.48$ nm for elongation and $\zeta_B = 1.59$ nm for fragmentation).

Structural transitions in filament growth: During filament growth by elongation, the incoming monomer has to undergo a conformational transition from the partially disordered state in bulk to the strand-loop-strand β-hairpin conformation in the bound state. In order to fit accurately onto the filament template, native hydrogen bonds must be formed between monomer and filament tip, while non-native hydrogen bonds have to be broken. Typical conformations along the free energy profile obtained from a cluster analysis for the three different growth processes are shown in Figure 2A-C. In agreement with experimental kinetic studies [16], our results show a wide spectrum of structures the monomer adopts during docking (snapshots in Figure 2A, B). Besides non-native contacts formed by 1-2 hydrogen bonds, (snapshot 6 in Figure 2A), short β-sheets with several non-native hydrogen bonds between the accessible filament tip and the monomer are observed to be a common structural motif upon docking (snapshot 5 in Figure 2A and snapshot 6 in Figure 2B). Various types of β-sheets are observed for the incoming monomer, including parallel and antiparallel as

13

well as in and out of register β-sheets. During the simulations in the intermediate region (0.6-0.8nm), a non-native hairpin structure is observed, consisting of correctly paired NT-strands of filament tip and monomer (parallel, almost in register) and a non-native, anti-parallel beta-sheet between the NT- and CT-strand of the incoming monomer (Supporting Information, Figure S7). A very similar intermediate hairpin structure has been found in previous implicit solvent simulation studies [24].

In the case of elongation at the even tip, initial contacts preferentially involve the CT strand of the monomer and the central hydrophobic region of the exposed N-terminal of the filament tip (vice versa for elongation at the odd tip). This agrees with the major pathway from recent studies using a coarse-grained hybrid-resolution model [27]. Note that in coarse-grained models, hydrogen bond formation is not included and we will discuss the important details on hydrogen bond formation in more detail further below.

During locking, the bound β-hairpin conformation initiates in the CT region (snapshot 3 in Figure 2A). Conformational changes upon binding of an additional monomer can be quantified in terms of the radius of gyration R_G and the distance root mean square deviation of the monomer's C_α-atoms (dRMSD) with respect to an idealized bound β-hairpin conformation (Figure 3A). For fragmentation, changes in the staggering of the associating hexamer are quantified by the nematic order parameter within each β-sheet and between the two sheets (Figure 3B). These order parameters are complemented by information on the secondary structure content in the bound and unbound state (top of Figure 3A, B). An analysis of types of secondary structures sampled along the monomer-filament separation coordinate indicates that coiled and bend secondary structure dominate in the intermediate and bulk distance range with small and fluctuating amounts of β and α helical conformations (Supporting Information, Figure S8). Monomeric Aβ in bulk can hence be regarded as a disordered, highly flexible peptide without a well-defined three-dimensional structure, but with a preference for some conformations. These findings are in agreement with experimental studies which classify monomeric Aβ as a partially disordered peptide with a collapsed structure [52](see minimum in R_G and maximum in coil content in secondary structure in Figure 3A).

The calculated bulk values of R_G around 0.9-1.1 nm are in good agreement with the range of 0.9-1.2 nm obtained from various simulation studies using different force fields [53–55]. Furthermore, the simulated R_G agrees with the hydrodynamic radius of 0.9±0.1

14

nm obtained from single-molecule fluorescence [56]. In the intermediate region, the initially compact monomer unfolds and forms non-native hydrogen bonds with the filament (increase in R_G). In the bound state, the monomer adopts a β-hairpin conformation, evident from the minimum in C_α-dRMSD, the maximum in R_G, and increase in β-sheet content (Figure 3A). The analysis of umbrella sampling windows reveals sampling of a broad distribution of dRMSD, R_G and monomer end-to-end distances in the intermediate and bulk regions indicating that a broad variety of conformations is sampled in these regions (Supporting Information, Figure S9). Very similar distributions are obtained from simulations with different monomeric starting conformations (β-hairpin with stagger 0 or 1 instead of 2, see Supporting Information, Figure S10 and S11). The conformational changes of the monomer at the odd tip are essentially identical (data not shown).

The situation is different for the assembly of two hexamers, since the two hexamer fragments maintain their cross-β structure in the growth process, evident from the constant β-sheet content and constant $\overline{P}_2$ within the NT- and CT-sheet (Figure 3B) or snapshot 4 in Figure 2C. However, the NT and CT regions slide against each other, resulting in a loss of the +2 staggering and a decrease in the total $\overline{P}_2$ (Figure 3B). Compared to protofilament elongation, the minor loss of conformational entropy upon fragment association may contribute to the significantly larger binding free energy. For the monomer (hexamer), the largest changes in the conformation occur at a short separation around $\zeta_c \sim 1.3$ ($\zeta_c \sim 2.3$ nm) between peptide and filament where the native hydrogen bonds start to form. The increased disorder around the fibril breakage site has been quantified in terms of a dRMSD per monomer from the bound conformation and shows decreasing disorder of monomers with decreasing the distance from the break site (see Supporting Information, Figure S12). Similar results have been obtained in previous simulation studies [57, 58].

Native and non-native hydrogen bond formation: Hydrogen bonds between the filament and the incoming monomer are important since they provide a directed force for the monomer to find its way from the partially disordered conformation in the unbound state to the highly ordered strand-loop-strand conformation in the bound state. For elongation at the even tip, Figure 4A shows the number of hydrogen bonds between filament and monomer as well as hydrogen bonds within the monomer. In the bound state, there are

on average 20 native hydrogen bonds and their number decreases rapidly with increasing separation ζ between filament and monomer. This loss of interface hydrogen bonds upon dissociation is partially compensated by the gain in intra-peptide hydrogen bonds. Due to the partially disordered character of the $A\beta$ peptide in bulk, these intra-peptide hydrogen bonds show larger fluctuations compared to the interface hydrogen bonds (see the larger standard deviations in Figure 4A).

In Figure 4B, the hydrogen bonds formed at certain separations between filament and monomer are further classified into native (green) and non-native (red) hydrogen bonds. At intermediate separations between monomer and filament ($1.3 < \zeta < 3$ nm), predominantly non-native hydrogen bonds are formed. During the initial docking step, these non-native contacts arise mainly between backbone residues in the CT region of the monomer and those in the central hydrophobic region (CHC) of the exposed NT region of the filament (see inset of Figure 4B, region 3). With decreasing separation between filament and peptide, more native hydrogen bonds are formed in the cross-over region (0.66 nm $< \zeta < 1.3$ nm). Here, the CT region of the peptide is already correctly folded and stabilized by native hydrogen bonds. However, the NT region of the peptide is kinetically trapped due to several non-native contacts (see inset of Figure 4B, region 2). In order to reach the correctly folded bound state these non-native contacts have to be broken. Breaking these non-native contacts in the cross-over region takes considerably longer compared to the docking region and the simulations indicate that the lifetime of individual hydrogen bonds can exceed a hundred nanoseconds (Figure 4C). This kinetic trapping of intermediate conformations has important consequences for filament growth since it drastically slows down the kinetics at short separations between filament and peptide as we will discuss in more detail further below.

The situation is similar for elongation at the odd tip and similar sequence regions are involved in the formation of non-native hydrogen bonds. For elongation at the odd tip, however, the non-native hydrogen bonds are formed between the CHC region of the NT of the monomer and the exposed CT of the filament (see Supporting Information, Figure S13). For fragmentation, initial interactions involve the solvent exposed parts of the two hexamers, for example the NT region of the hexamer to the left and the CT of the hexamer to the right (snapshot 4 in Figure 2C).

For the even tip, Figure 4C gives a schematic representation of the backbone position

or side chain involved in the hydrogen bond formation for three different separations. The majority of native and non-native hydrogen bonds corresponds to backbone hydrogen bonds (solid lines). Side chain hydrogen bonds arise between charged or polar amino acids, in particular between residues D23 and K28, which corresponds to the first stable native hydrogen bond formed in the crossover region (dashed green line in Figure 4C2). The predominance of backbone hydrogen bonds indicates a general, sequence independent mechanism of fibril growth. Even the first non-native hydrogen bonds formed during docking correspond to backbone hydrogen bonds and may thus hint at the dock/lock mechanism being a general feature of amyloid formation. At the same time, the first non-native contacts preferentially involve the CHC region of NT-strands and the mainly hydrophobic CT-strands, indicating a sequence-modulated propensity of fibril formation. These findings are in agreement with experiments observing a reduced fibril formation after substituting the CHC region by hydrophilic amino acids [59, 60].

Hydration layer: In addition to the conformational changes of peptide and filament, water molecules are expelled in the assembly process to create a dry interface between the filament and the peptide. Interestingly, it has been shown in previous simulations on short fragments that the lock step coincides with the creation of a dry interface between filament and incoming monomer and the the expulsion of water molecules [26]. Upon binding, a large part of the hydration layer surrounding the filament and monomer has to be striped off in order to create a dry binding interface and to facilitate peptide-peptide hydrogen bond formation (see snapshots for different filament-peptide separations in Figure 5B). Upon binding of a single monomer to the filament about 60 water molecules that are initially tightly bound in the hydration layer are released (Figure 5A), enhancing the entropy of the solvent. For the association of two hexamers, about 85 water molecules are released. The release of water molecules from the hydration layer to bulk is in congruence with a decrease in solvent accessible peptide surface area (SAS) from unbound to bound state. For elongation, the SAS decreases by 15 nm^2. Fragment association yields a more pronounced decrease of 21 nm^2.

In order to gain a better insight into the role of water in the binding process, we analyze the dynamics of the hydration water in the filament binding site. The lateral diffusion coefficient D_{lat} of the water molecules in the binding site of the filament is lower by a factor of 2 compared to bulk water (Figure 5C). This decrease in water mobility close to the binding site has two important consequences: Firstly, the collective motion of water molecules to

17

create a dry binding interface for the incoming peptide is slow. Secondly, the conformational changes of the peptide close to the filament are further retarded. A similar decrease in water mobility has been reported for various biological systems including lipid bilayers [61] and protein binding sites [62].

Energetics of filament growth: In the following, we analyze the energetics of filament growth and calculate the enthalpy difference $\Delta H = H_{\text{bound}} - H_{\text{unbound}}$ between the bound state and the unbound state (see Figure 6A for an illustration of the two states). The forces driving filament growth result from non-covalent interactions, mainly due to direct peptide-peptide interactions and solvation effects. In order to gain insight into these interactions, we calculate the energetic contributions to ΔH stemming from peptide-peptide interactions and from solvation effects due to peptide-solvent and solvent-solvent interactions with $H \approx U_{\text{PP}} + U_{\text{PS}} + U_{\text{SS}} + pV$. These individual contributions can be positive or negative, i.e. energetically promoting the unbound or the bound state and partially cancel out one another (Figure 6B).

The total enthalpy difference ΔH and the free energy difference ΔG allow an estimation of the entropic contribution $-T\Delta S = \Delta G - \Delta H$ (Figure 6C). Anticipating that hydrogen bonding is a key contributor to these energetic changes, we determine changes in hydrogen bond population upon binding, $\Delta n_{\text{hb}} = n_{\text{hb}}^{\text{bound}} - n_{\text{hb}}^{\text{unbound}}$, resolved by the participating species, as shown in Figure 6D.

For elongation, the peptide-peptide contribution is close to zero (slightly negative at the even and slightly positive at the odd tip). Favorable interactions due to the gain of up to 10 peptide-peptide hydrogen bonds in the bound state are compensated by the energetically disfavored strand-loop-strand conformation. For fragmentation, the peptide-peptide contribution is positive resulting from the large energy gain due to the loss of staggering (i.e. the sliding of NT and CT region against each other) in the unbound state. This gain amounts to 317 $k_{\text{B}}T$ compared to the ideal cross-β structure.

The peptide-solvent contributions are positive for all growth processes (unbound state favored), while the solvent-solvent interactions are negative (bound state favored), similar to the adsorption behavior of short peptide chains at different surfaces in contact with water [63]. These trends can be related to the gain of peptide-solvent hydrogen bonds in the unbound state and the gain of water-water hydrogen bonds in the bound state (Figure 6D). For fragment association, the peptide-solvent and solvent-solvent contributions are larger

18

compared to the elongation results since association involves a larger number of released hydration molecules.

In general, the individual energetic contributions are much larger than the resulting total enthalpy change due to the compensation of solvent and peptide interactions. Moreover, the change in total average number of hydrogen bonds between bound and unbound state is about zero (see Figure 6D). This almost perfect compensatory hydrogen bond mechanism has also been reported in simulation studies on amyloid formation of short model peptides [64, 65].

To summarize, filament growth by monomer addition or association of larger fragments is always favored ($\Delta G < 0$). The individual energetic contributions of peptide and solvent to the total enthalpy and to the total number of hydrogen bonds largely cancel out. Therefore, direct peptide-filament and peptide self-interactions (summarized in U_{PP}) and solvation effects (included in U_{PS} and U_{SS}) are important and have to be taken into account to quantitatively describe fibril growth. Coarse-grained or implicit solvent model might therefore predict a too strong energetic preference for assembly and entropic contributions are hidden in effective solute-solvent interaction terms. Overall, our results reveal that elongation and association are slightly disfavored by enthalpy ($\Delta H \gtrsim 0$). Filament elongation and association are therefore driven by entropy, which becomes evident from the large gain of entropy in the bound state ($-T\Delta S < 0$) in Figure 6C. This result seems surprising at first, since the transition of a disordered monomer in bulk to an ordered fibrillar conformation is associated with a reduction of the monomer's degrees of freedom and hence a loss of entropy. This loss of peptide entropy, however, is overcompensated by the gain of solvent entropy. The latter is related to the release of about 60 water molecules (85 for fragmentation) that are initially tightly bound in the first hydration layer around peptide and filament. As a consequence of an entropy driven assembly process, we predict a stabilization of the bound state with increasing the temperature. This prediction is in agreement with recent experimental results, which predict a shift towards the bound state indicated by an eight times higher equilibrium constant at 37 °C compared to 24 °C for $A\beta_{1-40}$ [16].

Kinetics of filament growth: We now turn to the kinetic aspects of filament growth. In our theoretical framework, the combination of the free energy profile $G(\zeta)$ and the diffusion profile $D(\zeta)$ uniquely determines the kinetics of filament growth. In the following, we first discuss the diffusion profiles $D(\zeta)$ for the three different growth processes. Then, we

19

use $D(\zeta)$ and $G(\zeta)$ to estimate rate constants and provide a detailed comparison to experimental results. Finally, we condense the information contained in $D(\zeta)$ and $G(\zeta)$ into one rescaled free energy profile that reflects the characteristic dock/lock mechanism of amyloid fibril growth.

Figure 7 shows the position-dependent diffusion profiles for filament elongation at the even tip and the odd tip (Figure 7A, D) and for association of two hexamers (Figure 7G) along the peptide-filament separation coordinate ζ. At large separations, the calculated diffusion profiles are constant as expected and the value for the monomer ($D_{\mathrm{unbound}} = 0.0003$ nm^2/ps) is in reasonable agreement with experimental results for $A\beta_{1-40}$ ($D_{\mathrm{unbound}} = 0.00015$ nm^2/ps [66]). Note that our filament model neglects residues 1-8, which may explain the slightly larger calculated diffusion coefficient. For smaller separations, the diffusion profiles show considerable variation along ζ. In particular, $D(\zeta)$ drops by several orders of magnitude indicating an important influence of orthogonal degrees of freedom on the kinetics. From our preceding analysis of conformations, hydrogen bonding and water mobility, we conclude that the three key degrees of freedom responsible for the retardation of the dynamics at close peptide-filament separations can be summarized as follows: (i) Conformational changes of the monomer from the partially disordered conformation in the unbound state to the highly ordered β-hairpin conformation in the bound state. These conformational changes are further retarded by the reduced water mobility in the binding site. (ii) Collective motion of water molecules with reduced mobility necessary to create a dry binding interface between monomer and filament. (iii) Formation of kinetically trapped conformations due to long-lived non-native hydrogen bonds in the crossover region. Indeed, the onset of the calculated diffusivity reduction coincides with a crossover of non-native to native hydrogen bond formation around $\zeta_C = 1.3$ nm (Figure 4B). The estimated changes in the diffusion profiles are of similar magnitude for the different growth processes although the types of conformational changes are different. Apparently, the timescale of folding single monomers is similar to the magnitude of the more global changes observed during the association of larger fragments, as reflected in the similar binding times.

The diffusion and free energy profiles can be used to estimate the kinetic rates according to Eq. 11 and 13. The rates and equilibrium constants for elongation/dissociation of a single monomer at the two filament tips and for association/fragmentation of hexamers are summarized in Table I. The calculated off rates at the even filament tip ($1.7 \cdot 10^{-1}$ s^{-1}) and

at the odd tip ($4.9 \cdot 10^{-2}$ s^{-1}) agree quite well with experimental results for Aβ_{1-40} (0.6 s^{-1}) obtained from hydrogen/deuterium exchange [67]. They are also consistent with the results of kinetic experiments on Aβ_{1-42} [14] ($1 \cdot 10^{-2}$ s^{-1}). The calculated association rate is on the edge to the diffusion limit ($6.8 \cdot 10^{9}$ M^{-1}s^{-1} for monomer, $4 \cdot 10^{9}$ M^{-1}s^{-1} for hexamer) and is two orders of magnitude higher compared to experimental results [12, 16]. However, similarly high elongation rates have been reported for ultrafast propagation in oligomeric clouds [68]. With the current approach, we likely overestimate k_{+} and k_{EQ} which is also evident from the larger binding free energy compared to experimental results. Note that the accuracy of the calculated rates depends exponentially on the free energy profile and only linearly on the diffusion profile. Large errors in the diffusion profile are therefore less decisive while errors of a few $k_B T$ in the free energy profile lead to high uncertainties in the calculated rates. A high accuracy in the free energy calculation is needed for reliable results. Based on the calculated rates and equilibrium constants for elongation and fragmentation, we can now predict the rate for primary nucleation according to Eq. 14. The nucleation rates calculated from our simulation data are larger than the experimental result obtained for Aβ_{1-42} ($k_n = 3 \cdot 10^{-4}$ M^{-1}s^{-1}) [14], by a factor of 10-100.

The dock/lock mechanism has been proposed previously for Aβ fibril growth based on kinetic experiments [8, 10, 12, 16] and has been supported by simulations of short model peptides consisting of a few amino acids [26, 28]. In the following, we demonstrate that this characteristic mechanism is well reflected by our methodology based on atomistic simulations of Aβ_{9-40} peptides. To gain insight into the full kinetic pathway of Aβ-fibril growth by monomer addition or hexamer assembly, we condense all kinetic information into one general free energy profile $\tilde{G}(q)$. So far, all the kinetic information is contained in the peptide-filament separation ζ, the free energy profile $G(\zeta)$ and the diffusion profile $D(\zeta)$. However, by choosing an appropriate transformation for all three and exploiting the kinetic quasi-universality of the Fokker-Planck equation, the kinetics of fibril growth remains unchanged [46]. For convenience, we choose the transformation such that the diffusion profile becomes constant, $D = D_{\text{unbound}}$ (Eq. 4). Therewith, regions of peptide-filament separations in which the dynamics is slow are stretched in the generalized coordinate q and previously hidden barriers appear in the rescaled free energy profile $\tilde{G}(q)$ that contains all the kinetic information of fibril growth.

Figure 7 shows the rescaled free energy profiles and the mean first passage times for

binding $\tau_{\mathrm{on}}(q)$ and for unbinding $\tau_{\mathrm{off}}(q)$ as a function of the generalized coordinate q, relative to the total binding time τ_{b} or unbinding time τ_{ub}. The values for τ_{b} and τ_{ub} are provided explicitly for all three growth processes (insets in Figure 7C, F, I and Table I). At large separations between a single monomer and the even filament tip, the rescaled free energy profile changes rapidly at large q, corresponding to fast dynamics in the initial docking phase (Figure 7B). The fast dynamics during docking is also reflected in the insignificant amount of the total binding time used for the docking step (Figure 7C). Beyond the docking region, at the crossover point ζ_C, the rescaled free energy is rather flat and the binding time increases monotonically. Consequently, the dynamics in the locking step is much slower compared to the initial fast docking. The gray regions in Figure 7 indicate a timescale gap of $\tau_{\mathrm{dock}}/\tau_{\mathrm{lock}} \sim 10^{-4} - 10^{-2}$ between the initial fast changes in the docking region relative to the slow changes in the subsequent locking region in agreement with previous results [27]. The situation is similar for fibril growth by elongation of a single monomer at the other fibril tip and also for the association of larger filament fragments: All three growth processes show the characteristic dock/lock mechanism and a timescale gap of several orders in magnitude. The results show that the crossover from docking to locking occurs around a peptide-filament separation of $\zeta_C = 1.3$ nm (even tip), $\zeta_C = 1.7$ nm (odd tip), and $\zeta_C = 3.2$ nm (hexamer). Interestingly, the binding times τ_b for fibril growth by a single monomer are similar to that of a hexamer fragment (inset of Figure 7). It is likely that the pre-ordering of the binding interfaces, which favors fast association, compensates for the larger size of the hexamers, which slows down diffusion. The results for the different fibril tips indicate a slightly preferred growth at the odd fibril tip that might lead to unidirectional growth of amyloid fibrils similar to insulin fibrils [69]. In contrast to the similar binding times, the unbinding time for two fragments is significantly larger compared to a single monomer. On the contrary this means that once a fibril is assembled, fibril breakage is extremely rare and the fully assembled fibrils do not serve as a reservoir for oligomers.

CONCLUSION

The dynamic pathway and the molecular mechanism of amyloid fibril formation is still not completely understood, while of great importance for the design of drug molecules that interfere with the process. Using $A\beta_{9-40}$ peptides as a model system, we systematically in-

vestigate the three growth processes that determine the kinetics of fibril growth: Elongation by a single monomer at the structurally unequal filament tips and the association of two larger filament fragments. Applying extensive MD simulations with explicit water provides insight into the molecular steps and driving forces underlying amyloid growth and allows us to extract kinetic information including macroscopic growth rates.

The free energy profiles underlying fibril growth indicate an onset of interactions already at monomer-filament separations > 2.5 nm that efficiently catch the approaching monomer or fragment and guide it towards a docking regime of association. The initial interactions involve mainly transient non-native hydrogen bonds and are possible due to the high conformational flexibility of Aβ peptides. Following initial docking, the association process is characterized by a continuous drop in free energy upon further distance decrease towards the fully bound state. This decrease in free energy is accompanied by a continuous increase of native hydrogen bonds at the cost of non-native hydrogen bonds. This detailed insight into the role of hydrogen bond formation in amyloid growth has not been feasible from coarse-grained simulations and elucidates the fundamental role of hydrogen bonds to mediate initial interactions, to guide the peptide to the ordered strand-loop-strand conformation in the bound state and to kinetically trap intermediate states.

To yield converged results for the free energy profiles, we propagate much longer trajectories compared to previous explicit solvent MD simulations [51] which allow us to achieve a much closer agreement with experimental binding free energies. These long simulations are necessary to sample the large conformational space of the partially disordered Aβ-peptide and to account for the slow relaxation in the binding process. The dock-lock binding mechanism and conformational intermediates like a non-native hairpin structure are in good agreement with implicit and coarse-grained simulations [24, 27], providing further confidence in our results.

The binding free energy of two ordered hexamer fragments is much larger compared to a single monomer. Therefore, ligands with conformational freedom as restricted as filament fragments could be effective competitors for Aβ monomers and could form the basis of amyloid inhibitor design [70]. The free energy for the assembly of two hexamer fragments demonstrates that partial disruptions of the filament are possible at relatively modest changes of free energy, especially in the N-terminal region. Hence, small drug molecules

could intercalate into a filament, partially disrupting its cohesion and in turn hindering further filament growth.

The energetic and entropic forces driving filament formation reveal that filament elongation is overall energetically disfavored. Moreover, an energetic decomposition reveals a near cancellation of individual contributions. Direct peptide-peptide interactions and solvation effects are therefore equally important and essential to quantitatively describe fibril growth, limiting the predictive power of implicit solvent and coarse-grained simulations. Overall, fibril formation is driven by entropy due to the increase of solvent entropy upon monomer or fragment binding to the filament tip, overcompensating the reduction of conformational entropy of the binding partners. The entropic preference of filament formation explains the observed increase of the amyloid stability with temperature [16].

Atomistic level investigation of $A\beta_{40}$ fibril growth remains tremendously challenging with current technologies due to the large system sizes and long timescales involved. To overcome the computational time scale limit, we extract kinetic information from our simulations by calculating the position-dependent diffusion profile for the approaching monomer or fragment. In our theoretical framework, we combine the detailed information contained in the diffusion profile and the free energy profile to describe the dynamics of fibril growth. The resulting dynamic pathway reveals that the initial docking is much faster compared to the subsequent locking in agreement with experimental predictions [8]. For fibril growth, both by single monomers and by association of larger fragments, the locking step is at least two orders of magnitude slower compared to docking. The significant retardation of the growth dynamics during locking at close separations between incoming peptide and filament arises in part from long-lived non-native hydrogen bonds, resulting in kinetically trapped intermediate states. Fibril growth additionally requires the collective motion of up to 85 water molecules to create a dry binding interface. This hydration water is much less mobile than molecules in bulk, as evidenced by a two-fold decrease in the diffusion coefficient, resulting in a slow expulsion of water upon assembly and a retardation of conformational changes close to the binding site. Therewith, water plays a decisive role in amyloid formation as entropic driving force and due to its influence on the growth dynamics.
Still, the slowest time scale in the locking step is most likely connected to the long time it takes to break several non-native hydrogen bonds, which can be on the order of 10 μs to 1 ms in peptide bundles [71].

SUPPORTING INFORMATION

Further discussions of fibril stability, potentials of mean force, energy decomposition, diffusion coefficients, and conformational changes. This material is available free of charge via the Internet at http://pubs.acs.org.

ACKNOWLEDGEMENTS

[1] Dauer, W.; Przedborski, S. *Neuron* **2003**, *39*, 889–909.

[2] DiFiglia, M.; Sapp, E.; Chase, K.; Davies, S.; Bates, G.; Vonsattel, J.; Aronin, N. *Science* **1997**, *277*, 1990–1993.

[3] Hardy, J.; Selkoe, D. J. *Science* **2002**, *297*, 353–356.

[4] Petkova, A. T.; Ishii, Y.; Balbach, J. J.; Antzutkin, O. N.; Leapman, R. D.; Delaglio, F.; Tycko, R. *Proc. Natl. Acad. Sci. USA* **2002**, *99*, 16742–16747.

[5] Petkova, A.; Leapman, R.; Guo, Z.; Yau, W.; Mattson, M.; Tycko, R. *Science* **2005**, *307*, 262–265.

[6] Buchete, N.-V.; Tycko, R.; Hummer, G. *J. Mol. Biol.* **2005**, *353*, 804–821.

[7] Buchete, N.-V.; Hummer, G. *Biophys. J.* **2007**, *92*, 3032–3039.

[8] Esler, W. P.; Stimson, E. R.; Jennings, J. M.; Vinters, H. V.; Ghilardi, J. R.; Lee, J. P.; Mantyh, P. W.; Maggio, J. E. *Biochem.* **2000**, *39*, 6288–6295.

[9] Kusumoto, Y.; Lomakin, A.; Teplow, D. B.; Benedek, G. B. *Proc. Natl. Acad. Sci. USA* **1998**, *95*, 12277–12282.

[10] Cannon, M. J.; Williams, A. D.; Wetzel, R.; Myszka, D. G. *Analyt. Biochem.* **2004**, *328*, 67–75.

[11] O'Nuallain, B.; Shivaprasad, S.; Kheterpal, I.; Wetzel, R. *Biochem.* **2005**, *44*, 12709–12718.

[12] Ban, T.; Yamaguchi, K.; Goto, Y. *Accounts Chem. Res.* **2006**, *39*, 663–670.

[13] Cohen, S. I. A.; Linse, S.; Luheshi, L. M.; Hellstrand, E.; White, D. A.; Rajah, L.; Otzen, D. E.; Vendruscolo, M.; Dobson, C. M.; Knowles, T. P. J. *Proc. Natl. Acad. Sci. USA* **2013**, *110*, 9758–9763.

[14] Meisl, G.; Yang, X.; Hellstrand, E.; Frohm, B.; Kirkegaard, J. B.; Cohen, S. I. A.; Dobson, C. M.; Linse, S.; Knowles, T. P. J. *Proc. Natl. Acad. Sci. USA* **2014**, *111*, 9384–9389.

[15] Buell, A. K.; Dhulesia, A.; White, D. A.; Knowles, T. P. J.; Dobson, C. M.; Welland, M. E. *Angew. Chem. Int. Ed.* **2012**, *51*, 5247–5251.

[16] Qiang, W.; Kelley, K.; Tycko, R. *J. Am. Chem. Soc.* **2013**, *135*, 6860–6871.

[17] O'Brien, E. P.; Okamoto, Y.; Straub, J. E.; Brooks, B. R.; Thirumalai, D. *J. Phys. Chem. B* **2009**, *113*, 14421–14430.

[18] Oosawa, F.; Kasai, M. *J. Mol. Biol.* **1962**, *4*, 10.

[19] Michaels, T. C. T.; Knowles, T. P. J. *J. Chem. Phys.* **2014**, *140*, 214904.

[20] Wu, C.; Shea, J.-E. *Curr. Op. Struct. Biol.* **2011**, *21*, 209–220.

[21] Fawzi, N. L.; Kohlstedt, K. L.; Okabe, Y.; Head-Gordon, T. *Biophys. J.* **2008**, *94*, 2007–2016.

[22] Fawzi, N. L.; Okabe, Y.; Yap, E.-H.; Head-Gordon, T. *J. Mol. Biol.* **2007**, *365*, 535–550.

[23] Takeda, T.; Klimov, D. K. *Biophys. J.* **2009**, *96*, 442–452.

[24] Gurry, T.; Stultz, C. M. *Biochem.* **2014**, *53*, 6981–6991.

[25] Santini, S.; Mousseau, N.; Derreumaux, P. *J. Am. Chem. Soc.* **2004**, *126*, 11509–11516.

[26] Nguyen, P. H.; Li, M. S.; Stock, G.; Straub, J. E.; Thirumalai, D. *Proc. Natl. Acad. Sci. USA* **2007**, *104*, 111–116.

[27] Han, W.; Schulten, K. *J. Am. Chem. Soc.* **2014**, *136*, 12450–12460.

[28] Schor, M.; Vreede, J.; Bolhuis, P. G. *Biophys. J.* **2012**, *103*, 1296–1304.

[29] Lam, A. R.; Rodriguez, J. J.; Rojas, A.; Scheraga, H. A.; Mukamel, S. *J. Phys. Chem. A* **2013**, *117*, 342–350.

[30] Bjelkmar, P.; Larsson, P.; Cuendet, M. A.; Hess, B.; Lindahl, E. *J. Chem. Theory Comput.* **2010**, *6*, 459–466.

[31] Jorgensen, W. L.; Chandrasekhar, J.; Madura, J. D.; Impey, R. W.; Klein, M. L. *J. Chem. Phys.* **1983**, *79*, 926–935.

[32] Erbas, A.; Horinek, D.; Netz, R. R. *J. Am. Chem. Soc.* **2012**, *134*, 623–630.

[33] Van Der Spoel, D.; Lindahl, E.; Hess, B.; Groenhof, G.; Mark, A. E.; Berendsen, H. J. C. *J. Comput. Chem.* **2005**, *26*, 1701 – 1718.

[34] Darden, T.; York, D.; Pedersen, L. *J. Chem. Phys.* **1993**, *98*, 10089–10092.

[35] Kumar, S.; Rosenberg, J. M.; Bouzida, D.; Swendsen, R. H.; Kollman, P. A. *J. Comput. Chem.* **1995**, *16*, 1339–1350.

[36] Kabsch, W.; Sander, C. *Biopolymers* **1983**, *22*, 2577–2637.

[37] Cecchini, M.; Rao, F.; Seeber, M.; Caflisch, A. *J. Chem. Phys.* **2004**, *121*, 10748–10756.

[38] Seeber, M.; Felline, A.; Raimondi, F.; Muff, S.; Friedman, R.; Rao, F.; Caflisch, A.; Fanelli, F. *J. Comput. Chem.* **2011**, *32*, 1183–1194.

[39] Shao, J.; Tanner, S. W.; Thompson, N.; Cheatham, T. E. *J. Chem. Theory Comput.* **2007**, *3*, 2312–2334.

[40] Hess, B. *J. Chem. Phys.* **2002**, *116*, 209.

[41] Hänggi, P.; Borkovec, M. *Rev. Mod. Phys.* **1990**, *62*, 251–341.

[42] Hummer, G. *New J. Phys.* **2005**, *7*, 34–34.

[43] Zhu, F.; Hummer, G. *J. Chem. Theory Comput.* **2012**, *8*, 3759–3768.

[44] Flyvbjerg, H.; Petersen, H. G. *J. Chem. Phy.s* **1989**, *91*, 461.

[45] Rhee, Y. M.; Pande, V. S. *J. Phys. Chem. B* **2005**, *109*, 6780–6786.

[46] Hinczewski, M.; von Hansen, Y.; Dzubiella, J.; Netz, R. R. *J. Chem. Phys.* **2010**, *132*, 245103.

[47] Best, R. B.; Hummer, G. *Proc. Natl. Acad. Sci. USA* **2010**, *107*, 1088–1093.

[48] Chandler, D. *Introduction to Modern Statistical Mechanics*; Oxford University Press: 198 Madison Avenue, New York, 1987.

[49] Weiss, G. H. *First Passage Time Problems in Chemical Physics*; Advances in Chemical Physics; John Wiley & Sons, Inc.: Hoboken, NJ, USA, 1967; Vol. 13.

[50] Houston, P. L. *Chemical Kinetics and Reaction Dynamics*; Courier Corporation, 2012.

[51] Lemkul, J. A.; Bevan, D. R. *J. Phys. Chem. B* **2010**, *114*, 1652–1660.

[52] Frieden, C. *Protein Sci.* **2007**, *16*, 2334–2344.

[53] Raffa, D. F.; Rauk, A. *J. Chem. Phys.* **2007**, *111*, 3789–3799.

[54] Massi, F.; Peng, J. W.; Lee, J. P.; Straub, J. E. *Biophys. J.* **2001**, *80*, 31–44.

[55] Baumketner, A.; Bernstein, S. L.; Wyttenbach, T.; Bitan, G.; Teplow, D. B.; Bowers, M. T.; Shea, J. E. *Prot. Sci.* **2006**, *15*, 420–428.

[56] Nag, S.; Sarkar, B.; Bandyopadhyay, A.; Sahoo, B.; Sreenivasan, V. K. A.; Kombrabail, M.; Muralidharan, C.; Maiti, S. *J. Biol. Chem.* **2011**, *286*, 13827–13833.

[57] Solar, M.; Buehler, M. J. *Nanotechnology* **2014**, *25*, 105703.

[58] Paparcone, R.; Buehler, M. J. *Biomaterials* **2011**, *32*, 3367 – 3374.

[59] Hamley, I. W. *Chem. Rev.* **2012**, *112*, 5147–5192.

[60] Hilbich, C.; Kisters-Woike, B.; Reed, J.; Masters, C. L.; Beyreuther, K. *J. Mol. Biol.* **1992**, *228*, 460–473.

[61] von Hansen, Y.; Gekle, S.; Netz, R. R. *Phys. Rev. Lett.* **2013**, *111*, 118103.

[62] Nibali, V. C.; Havenith, M. *J. Am. Chem. Soc.* **2014**, *136*, 12800–12807.

[63] Schwierz, N.; Horinek, D.; Liese, S.; Pirzer, T.; Balzer, B. N.; Hugel, T.; Netz, R. R. *J. Am. Chem. Soc.* **2012**, *134*, 19628–19638.

[64] Narayanan, C.; Dias, C. L. *J. Chem. Phys.* **2013**, *139*, 115103.

[65] Su, Z.; Dias, C. L. *J. Chem. Phys.* **2014**, *118*, 10830–10836.

[66] Tseng, B. P.; Esler, W. P.; Clish, C. B.; Stimson, E. R.; Ghilardi, J. R.; Vinters, H. V.; Mantyh, P. W.; Lee, J. P.; Maggio, J. E. *Biochem.* **1999**, *38*, 10424–10431.

[67] Sanchez, L.; Madurga, S.; Pukala, T.; Vilaseca, M.; Lopez-Iglesias, C.; Robinson, C. V.; Giralt, E.; Carulla, N. *J. Am. Chem. Soc.* **2011**, *133*, 6505–6508.

[68] Ogi, H.; Fukukshima, M.; Hamada, H.; Noi, K.; Hirao, M.; Yagi, H.; Goto, Y. *Sci. Rep.* **2014**, *4*, 6960.

[69] Heldt, C. L.; Zhang, S.; Belfort, G. *Proteins* **2011**, *79*, 92–98.

[70] Kapurniotu, A. *Angew. Chem. Int. Ed.* **2011**, *50*, 11293–11294.

[71] Erbas, A.; Netz, R. R. *Biophys. J.* **2013**, *104*, 1285–1295.

[72] Mahoney, M.; Jorgensen, W. *J. Chem. Phys.* **2001**, *114*, 363–366.

TABLE I. Equilibrium constant k_{EQ}, macroscopic rates k_{off} and k_+, nucleation rate k_{n} and microscopic unbinding τ_{ub} and binding times τ_{b} for $A\beta_{9-40}$ filament growth by addition of a single monomer to the even and odd filament tip or by the association of two hexamer fragments. The rates are calculated according to Eq. 11 and 13 with microscopic interaction range $\zeta_S = 3.0$ nm (monomer) or $\zeta_S = 3.8$ (hexamer) and $D = 0.0003$ nm/ps^2 (monomer) and $D = 2 * 0.00007$ nm/ps^2 (hexamer). The diffusion limit for monomer addition is $6.8 \cdot 10^9$ and $4.0 \cdot 10^9$ for hexamer association.

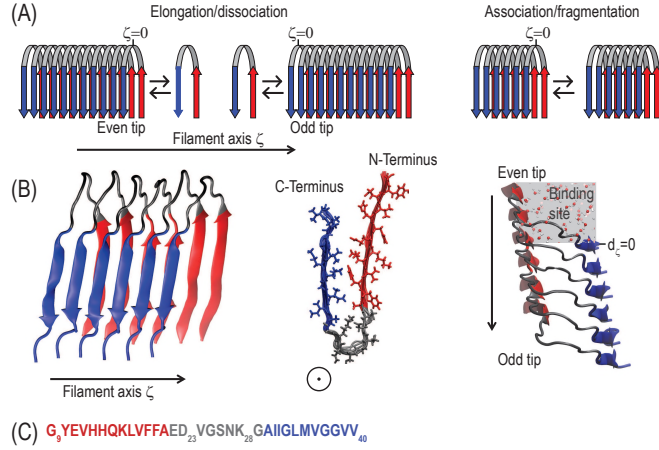| Monomer	k_{off} [s^{-1}]	k_+ [M^{-1}s^{-1}]	k_{EQ} [M^{-1}]	k_{n} [M^{-1}s^{-1}]	τ_{ub} [s]	τ_{b} [s]
even tip	$1.7 \cdot 10^{-1}$	$1.5 \cdot 10^9$	$8.7 \cdot 10^9$	$2.6 \cdot 10^{-3}$	4.67	$9.94 \cdot 10^{-6}$
odd tip	$4.9 \cdot 10^{-2}$	$3.3 \cdot 10^9$	$6.7 \cdot 10^{10}$	$4.4 \cdot 10^{-2}$	10.62	$2.3 \cdot 10^{-6}$
Hexamer						
	$1.8 \cdot 10^{-13}$	$1.9 \cdot 10^9$	$1 \cdot 10^{22}$	-	$2.95 \cdot 10^{12}$	$1.4 \cdot 10^{-6}$

FIG. 1. (A) Schematic representation of the growth processes for filament formation: Elongation/dissociation by one monomer at the even and at the odd tip and association/fragmentation of two hexamers. (B) Section of the cross-β structure of a Aβ_{9-40} filament based on experimental results and viewed from different perspectives. The regions are colored according to their secondary structure: N-terminal (NT) β-sheet (red), C-terminal (CT) β-sheet (blue) and loop region (gray). Due to the $+2$ staggering, the two filament ends are not identical and denoted as even tip (NT exposed) and odd tip (CT exposed). The gray region indicates the binding site at the even tip that is filled with water molecules. (C) Amino acid sequence of a single Aβ_{9-40} peptide. In (A), $\zeta = 0$ indicates the zero point used for the free energy profiles shown in Figure 2. In (B), $d_\zeta = 0$ indicates the CT-strand position of the peripheral peptide in β-hairpin conformation.
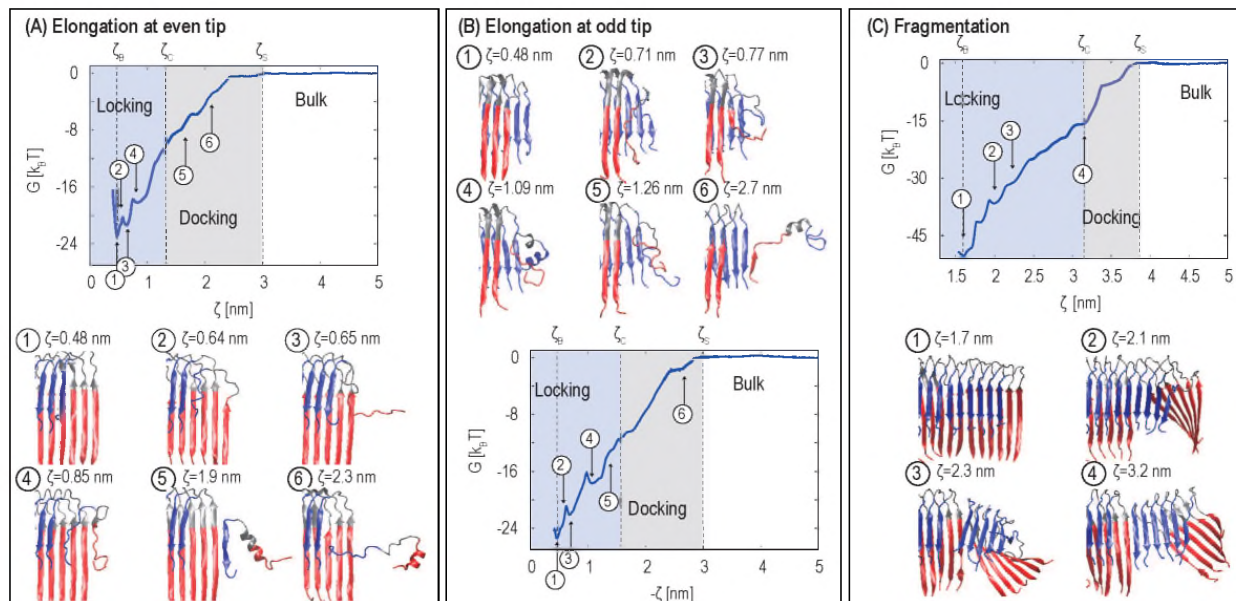
FIG. 2. Free energy profiles G in dependence the peptide-filament separation along the filament axis ζ and selected simulation snapshots resulting from our cluster analysis. (A) Filament elongation by a single monomer at the even tip, (B) elongation at the odd tip and (C) association of two hexamer fragments. In the snapshots, a small section of the filament is shown to the left and the binding monomer/hexamer is shown to the right. Water molecules are not shown for clarity. ζ_B indicates the position of the bound state (minimum in the profile in agreement with the inter-peptide spacing observed in the NMR structure). ζ_C indicates the peptide-filament separation for which we predict the crossover from the fast docking dynamics to the much slower locking dynamics (Figure 7). ζ_S indicates the beginning of the unbound state where the peptide is in solution and the filament-peptide interactions are zero.
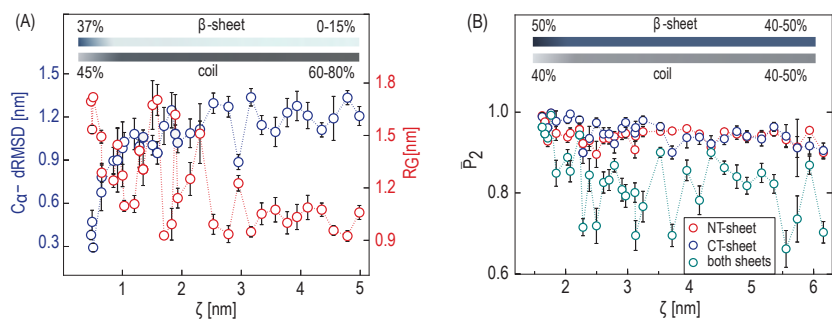
FIG. 3. (A) Conformational changes of the monomer during filament elongation at the even filament tip. The changes are characterized by backbone C_α-dRMSD with respect to the idealized β-hairpin conformation (blue) and radius of gyration R_G (red). (B) For fragmentation, the nematic order parameter $\overline{P}_2$ characterizes the peptide alignment in the NT and CT β-sheets and in both sheets of the associating hexamer. The secondary structure content of the monomer and hexamer is shown as inset at the top of Figure (A) and (B) in dependence of the separation ζ. The shading of the bars indicates the content of β-sheet and coil content and the numbers indicate the values in the bound and unbound state.
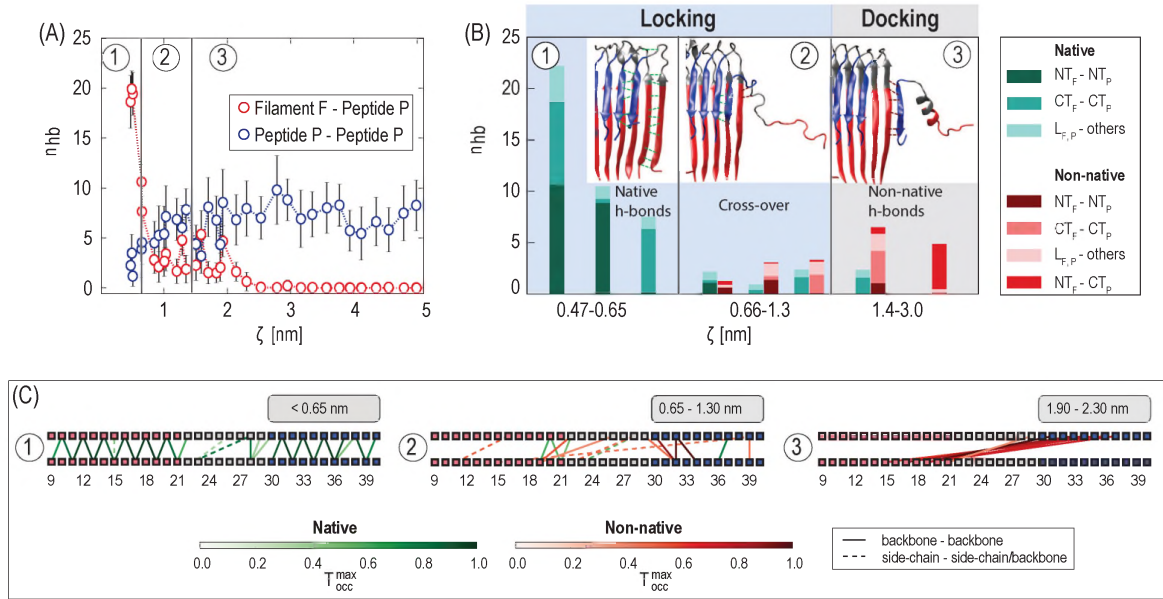
FIG. 4. (A) Average number of hydrogen bonds in dependence of the peptide-filament separation ζ at the even filament tip. Hydrogen bonds between the filament and peptide are shown in red, intra-peptide hydrogen bonds are shown in blue. (B) Classification of peptide-filament hydrogen bonds into native and non-native hydrogen bonds. The hydrogen bonds are further decomposed into the regions of NT or CT strand involved in their formation. Typical conformations are shown as insets in the three different regions: 1. Native hydrogen bond formation (bound state), 2. kinetically trapped conformation due to non-native hydrogen bonds in the crossover region, 3. non-native hydrogen bond formation during initial docking. (C) Schematic representation of the hydrogen bonds between filament and peptide resolving the backbone and side chain position of the bond for the three different regions. The bonds are colored according to their maximal lifetime T_{occ}^{max}.
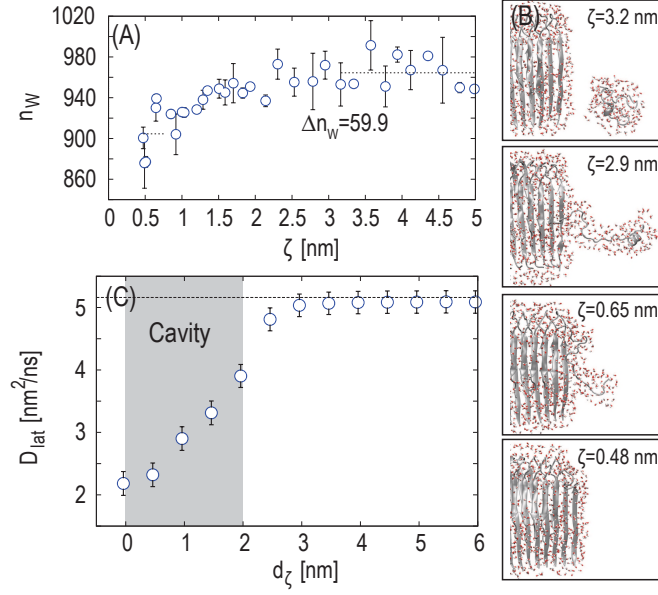
FIG. 5. Expulsion of water molecules to create a dry interface for monomer binding at the even filament tip. The total number of water molecules in the first hydration layer surrounding the filament and the incoming peptide are shown as function of the peptide-filament separation ζ (A). (B) Simulation snapshots of the hydration layer during monomer binding for selected separations ζ. All snapshots are taken after 50 ns and visualize the water molecules within a distance of 0.3 nm of the peptide and filament. (C) Lateral diffusion coefficient D_{lat} of the water molecules in the binding site (indicated by the gray region) in dependence of their position along the filament axis d_{ζ}. The dashed line corresponds to the bulk value for TIP3P water at room temperature [72].
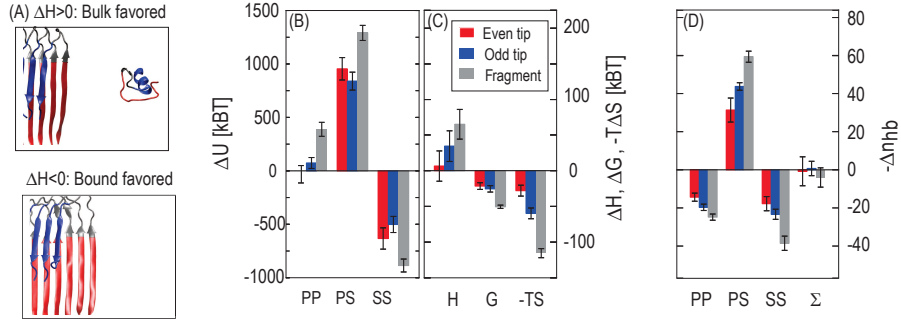
34

FIG. 6. Enthalpy and entropy differences between the bound state and the unbound state, defined as $\Delta H = H_{\text{bound}} - H_{\text{unbound}}$. (A) Illustration of the two states at the even tip. For $\Delta H < 0$, the bound state is energetically favored, while for $\Delta H > 0$, the unbound state is favored. (B) Decomposition of the enthalpy difference into energetic contributions from peptide-peptide, peptide-solvent and solvent-solvent interactions with $H \approx U_{\text{PP}} + U_{\text{PS}} + U_{\text{SS}} + pV$. The trends are similar for all three growth processes: Elongation at the even tip (red), at the odd tip (blue) and fragment association (gray). (C) Difference of the total enthalpy H, free energy G and entropic contribution $-TS = G - H$. (D) Difference of the number of hydrogen bonds $\Delta n_{\text{hb}} = n_{\text{hb}}^{\text{bound}} - n_{\text{hb}}^{\text{unbound}}$ for the individual contributions and the total system.
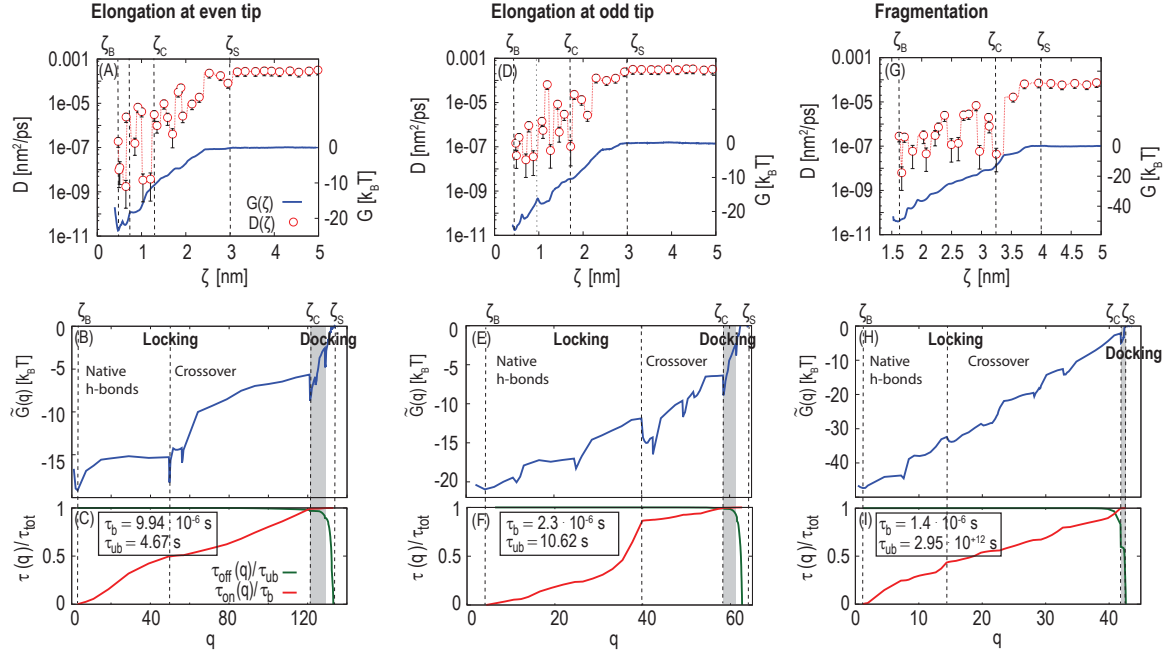
FIG. 7. Top row: Position-dependent diffusion profile $D(\zeta)$ and free energy profile $G(\zeta)$ along the peptide-filament separation ζ: (A) Elongation by monomer addition at the even tip, (D) elongation at the odd tip and (G) association of two hexamer fragments. Middle row: Rescaled free energy profiles $\tilde{G}(q)$ for a constant diffusion profile $D = D_{\text{unbound}}$ along the generalized coordinate q according to Eq. 4. The rescaled profiles contain the full kinetic information for fibril growth. Bottom row: Mean first passage time for binding $\tau_{\text{on}}(q)$ and for unbinding $\tau_{\text{off}}(q)$ dependent on the position q along the rescaled free energy profile $\tilde{G}(q)$. The values are given relative to the total binding time τ_{b} or unbinding time τ_{ub} (provided in the insets). The gray areas indicate a time scale gap of $\tau_{\text{dock}}/\tau_{\text{lock}} \sim 10^{-4} - 10^{-2}$ between the fast dynamics in the docking region and the slow dynamics in the locking region. ζ_C indicates the position for which we predict the crossover from docking to locking. ζ_B and ζ_S indicate the bound state and the unbound state, respectively.

Reduced water mobility

Trapping